Chapter 8

Numerical Experiments

8.1 Lid Driven Cavity Flow (2D)

A lid driven cavity is a very popular two dimensional test case. Figure 8.1 shows a sketch of the problem. A square computational domain is used for this test. The left, right and lower wall of the square represent physical walls. Thus no-slip condition will be prescribed for the simulation. For the upper boundary the velocity is set to u_∞. In 1982 Ghia [30] has performed a number of computations on rather fine grids, using the stream-function vorticity formulation of the Navier Stokes equations. These simulations shall be used as reference here. All geometric lengths in this paragraph are relativ to the size of the square cavity, which has the edge length 1. Different resolutions, using hybrid grids are to be compared. Figure 8.2 shows two grids from this series. Starting from a Cartesian base grid, all four boundaries have been anisotropically refined. The following table gives an overview over the grids, which have been used.

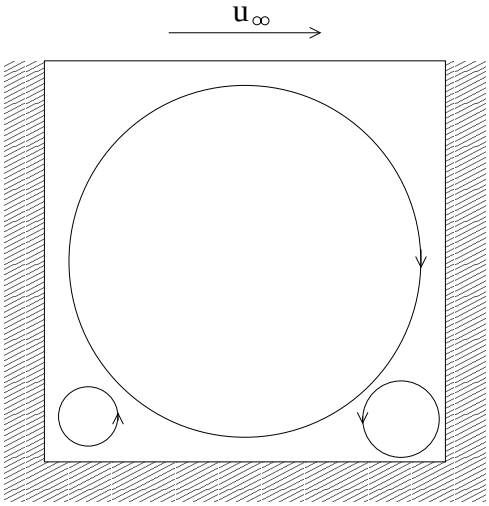

Figure 8.1: Lid driven cavity problem.

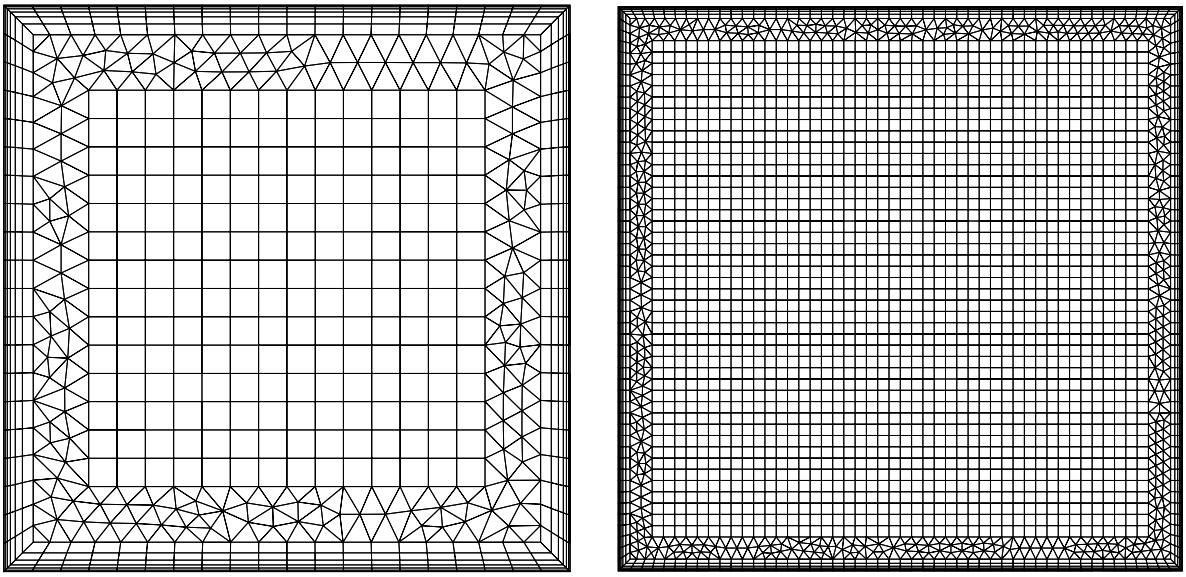

Figure 8.2: Grids for cavity problem (edge-length = 0.05 (left) and 0.02 (right)).

Overview over Grids for Lid Driven Cavity Test-Case

edge length	0.050	0.040	0.030	0.025	0.020	0.015	0.010	0.005	0.003
elements	1,046	1,441	2,279	2.920	4,190	6,749	13,426	47,046	123,491
triangles	370	480	746	804	1,054	1,392	2,192	4,610	8,477
quads	676	961	1,533	2,116	3,136	5,357	11,234	42,436	115,014
nodes	902	1,252	1,974	2,599	3,764	6,190	12,531	45,142	119,920
edges	1,947	2,693	4,252	5,518	7,953	12,938	25,956	92,187	243,410
% triangles	35%	33%	33%	28%	25%	21%	16%	10%	7%
% bd. elem.	62%	57%	51%	45%	40%	34%	26%	15%	10%
% bd. edges	57%	52%	46%	41%	36%	30%	22%	13%	8%
edges/nodes	2.16	2.15	2.15	2.12	2.11	2.09	2.07	2.04	2.03
$-u(\frac{1}{2}, \frac{1}{5}) \cdot 10^1$	3.486	3.597	3.744	3.818	3.824	3.803	3.754	3.739	3.734

All grids have been created, using an equidistant Cartesian mesh as starting point. The edge length in the above table refers to the edge length of the squares of this initial grid. The four walls of the cavity have been refined, using six layers of bilinear elements. The aspect ratio of the finest layer is 20 and it decreases by a factor of 1.5 towards the inner Cartesian grid. With increasing resolution, the percentage of triangles becomes significantly smaller. This effect is welcome, since bilinear elements, if properly aligned, offer a better approximation than triangles. The computational costs of a simulation are strongly dependent on the total number of edges. A fully triangulated mesh has approximately three times as many edges as nodes. For a grid consisting entirely of bilinear elements this ratio would be 2. Thus it is desireable to reduce the amount of triangles as much as possible. The connection between the boundary grid and the inner

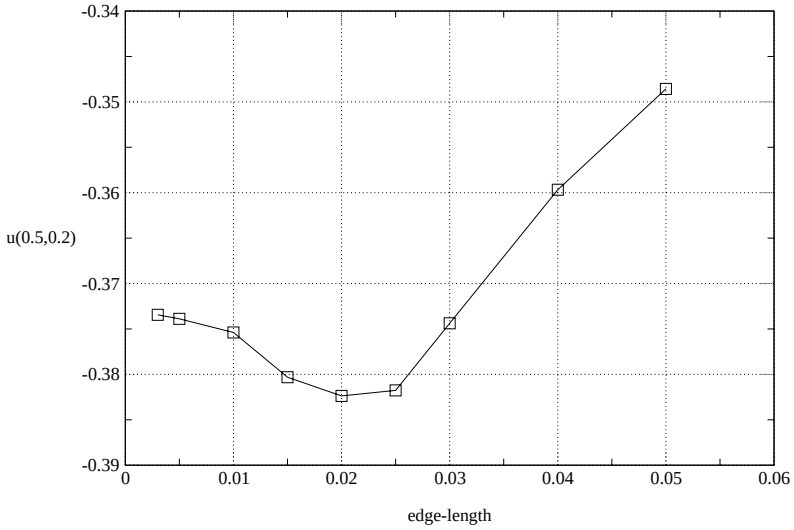

Figure 8.3: $u(0.5, 0.2)$ as function of the mesh-resolution.

Cartesian grid, however, introduces a thin triangular region. In the above tables values for *% bd.elem.* and *% bd. edges* can be found. These values show how many elements/edges are used in the boundary grid compared to the total number of elements/edges. They have been computed by differencing the number of elements/edges of the grid and the number of elements/edges a uniform Cartesian mesh with the same inner edge-length would have. To illustrate the influence of the resolution on the solution, values for u at $x = 0.5$ and $y = 0.2$ have been investigated. Figure 8.3 shows $u(0.5, 0.2)$ as a function of the mesh resolution. The difference from one grid to the next finer one decreases with an increasing resolution. This suggests, that the order of the numerical scheme is more than linear. Unfortunately it is not possible to estimate an order from figure 8.3. Figure 8.4 shows a comparion of the simulated data and the data to be found in [30]. The diagrams show u and v in a horizontal and a vertical cut through the middle of the cavity. Data which has been obtained on three different grids is shown. Please note that for grids with a smaller edge-length than 0.010 no difference could have been observed in the diagram. Thus the finer resolutions have been left out in order to improve the readability of the diagrams. Figure 8.5 shows an iso-plot of $\frac{|\mathbf{v}|}{|\mathbf{v}_\infty|}$ as well as stream-lines for this test-case. The iso-line levels range from 0 to 1 and they are set apart by 0.05.

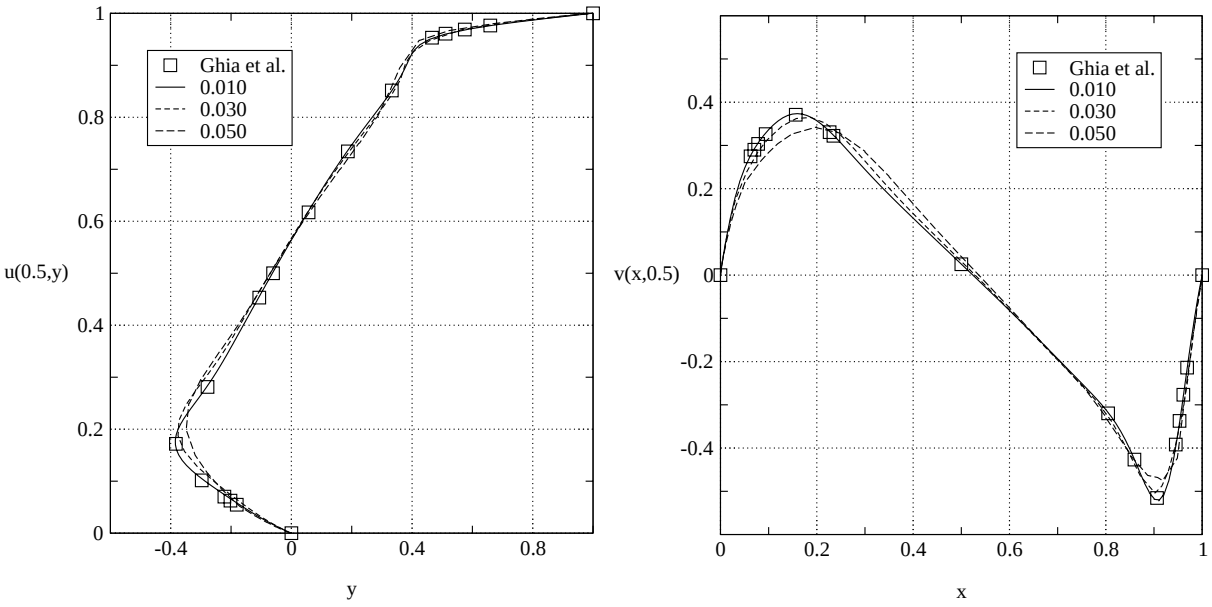

Figure 8.4: Comparison between computed results and [30].

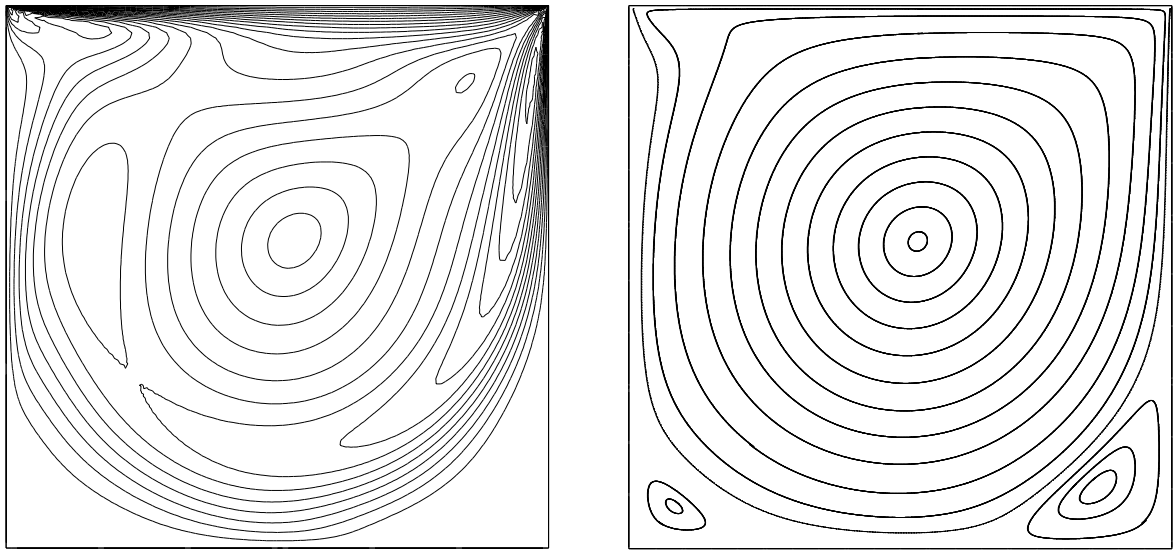

Figure 8.5: Iso-lines of $|\mathbf{v}|$ and stream-lines for cavity test-case ($Re = 1000$).

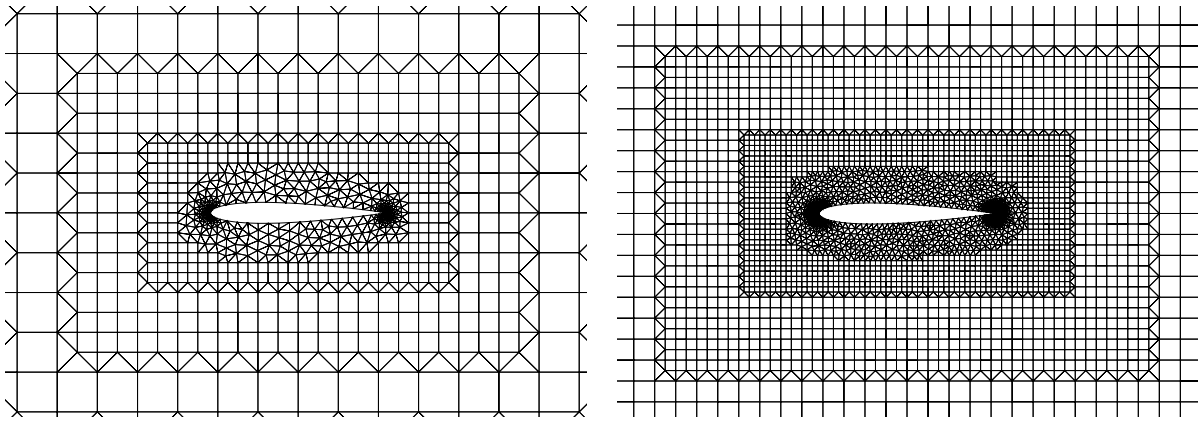

Figure 8.6: Two different grids (1.00 and 0.50) for the NACA-0012 tests.

8.2 Two-Dimensional Flow Around Airfoils

8.2.1 Accuracy Tests for Inviscid Flow

In order to test the accuracy of the inviscid part of the discretization, a series of computations for symmetric flow around a NACA-0012 airfoil have been performed. The quantity, which has been used as an error-measure, is the drag. Ideally this has to be zero in an inviscid computation. Four different grids, four different variable reconstructions and two different Mach-numbers have been investigated. A full upwind discretization with the following different reconstructions (see also 3.2.4) has been used.

- a simple first order approach (figure 3.14/a)
  index 1 in the following tables

- a formal second order approach (figure 3.14/b)
  index 2 in the following tables

- the above scheme, limited by van Albada's limiter
  index VA in the following tables

- a formal third order (along an edge) approach (figure 3.14/c)
  index 3 in the following tables

It has been tried to keep the grids similar to each other. Starting point was a Cartesian base grid. The edge length of this base grid, is what is given in the following comparison table. This base grid has been isotropically refined four times. Around the airfoil a triangular region can be found. This region has roughly the same size for all the grids. The leading and trailing edge have been locally refined again. Figure 8.6 shows two grids from this series.

Overview over Grids for NACA-0012 Airfoil

edge-length	1.00	0.75	0.50	0.25
elements	1,641	2,587	5,900	22,751
triangles	1,054	1,587	3,106	10,356
quads	587	1,000	2,764	12,395
nodes	1,164	1,858	4,441	17,759
edges	2,805	4,445	10,341	40,510
% triangles	64%	61%	53%	54%
edges/nodes	2.41	2.39	2.33	2.28

Overview over Results for NACA-0012 Airfoil

The two following tables show the different drag coefficients which have been computed.

Ma=0.01

edge-length	1.00	0.75	0.50	0.25	estimated order
c_{D_1}	0.03180	0.02699	0.01846	0.01030	0.80
$c_{D_{VA}}$	0.008356	0.004596	0.002232	0.0005344	1.97
c_{D_2}	0.004795	0.002857	0.001355	0.0004037	1.81
c_{D_3}	0.003920	0.002083	0.001150	0.0003410	1.89

Ma=0.5

edge-length	1.00	0.75	0.50	0.25	estimated order
c_{D_1}	0.03598	0.03055	0.02066	0.01141	0.81
$c_{D_{VA}}$	0.01017	0.005923	0.002591	0.0006054	1.95
c_{D_2}	0.004573	0.002263	0.001155	0.0003355	2.14
c_{D_3}	0.003700	0.001963	0.001002	0.0002987	2.01

The order has been estimated with the help of a numerical curve fit, using an ansatz of the following form:

$$c_D = a_1 h^{a_2} . \tag{8.1}$$

h denotes the edge length and the exponent a_2 gives an estimate for the numerical order. Figure 8.7 shows a comparison of the results and figure 8.8 a convergence history of the formal third-order computations ($Ma = 0.5$). It can be observed, however, that this is actually second order accurate. Although the values for c_D are a little better than what has been obtained with the standard second order scheme.

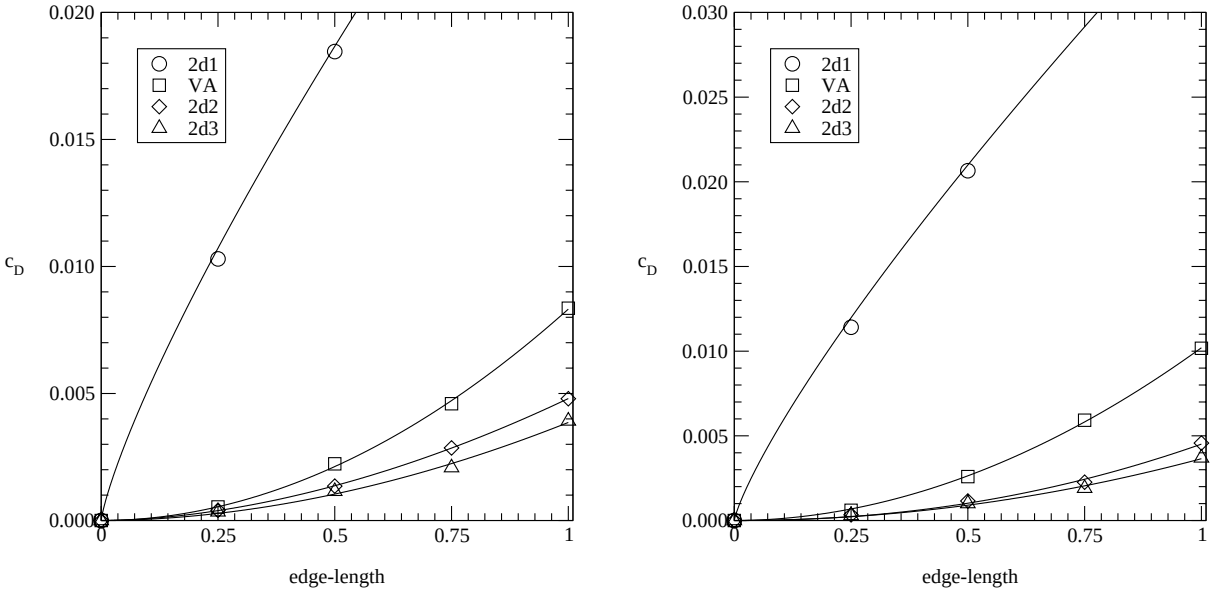

Figure 8.7: Drag-coefficients.

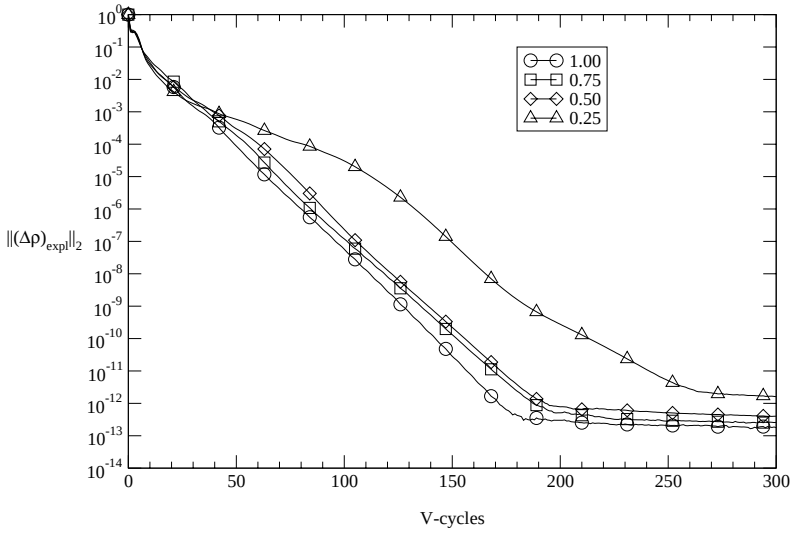

Figure 8.8: Convergence history.

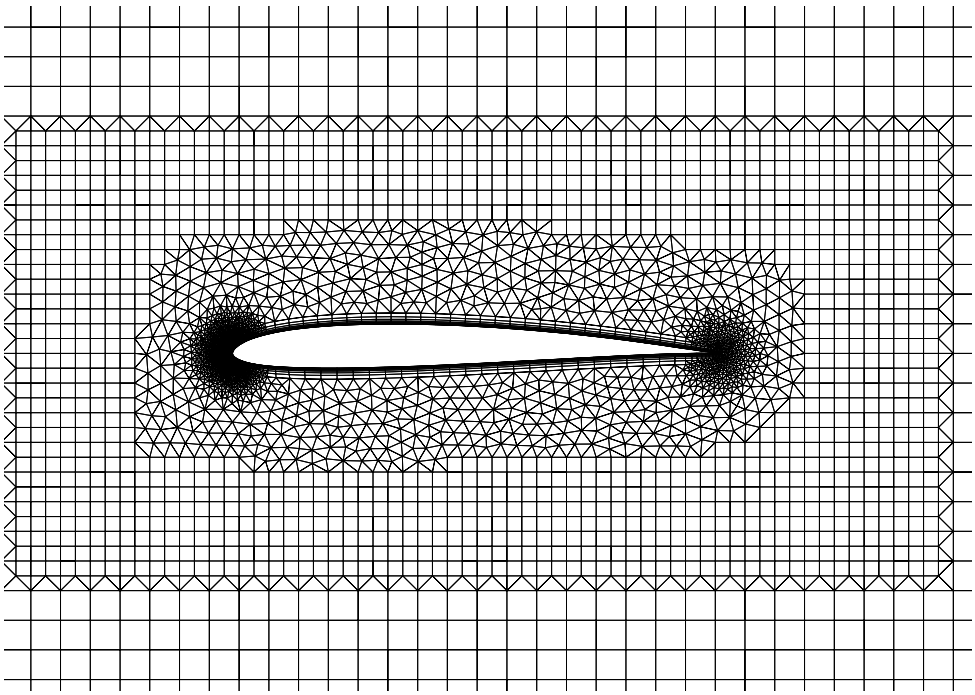

Figure 8.9: Mesh for an SD8000 airfoil.

8.2.2 Viscous Flow Around a Selig/Donovan SD8000 Airfoil

The flow around a Selig/Donovan SD8000 low Reynolds number airfoil has been computed for different angles of attack, ranging from $-3°$ to $+8°$. A Reynolds number of $Re = 5,000$ and a Mach number of $M = 10^{-3}$ has been used. Figure 8.9 shows the computational grid, which has been used for the simulations. It is a hybrid grid, which has been created using the algorithm descibed in chapter 4. In figure 8.11 velocity isolines can be seen for an angle of attack of $5°$. This is roughly the optimum, which results in an approximate glide ratio of 10. Nevertheless a seperation appears, which can be seen in figure 8.12, which shows stream lines around the airfoil for an angle of attack of $5°$. Please note that the Reynolds number is fairly low and thus the viscous effects drastically increase the drag. A polar diagram, resulting from the simulations, can be seen in figure 8.12.

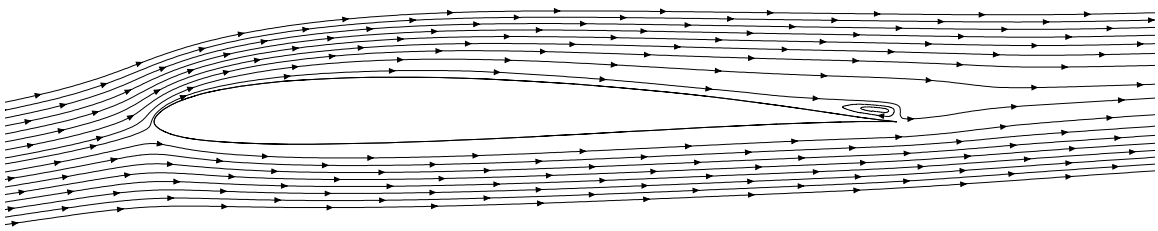

Figure 8.10: Stream-lines ($Re = 5000$ and $\alpha = 5$).

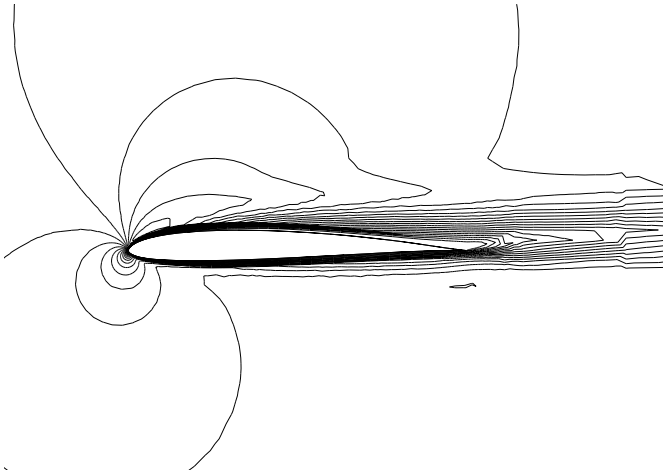

Figure 8.11: Iso-lines of $|v|$.

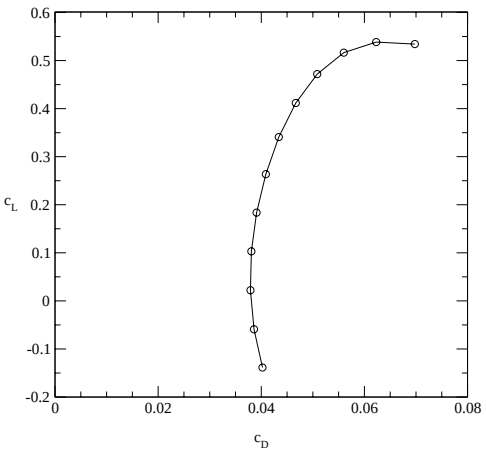

Figure 8.12: Polar diagram.

8.2.3 Inviscid, Transsonic Flow Around an RAE2822 Airfoil

Here the results of an inviscid simulation of transsonic flow shall be compared to experimental data. Flow around an RAE-2822 transsonic airfoil shall be computed. The free-stream Mach number is 0.729 and the angle of attack 2.31°. Experimental data can be found in [31] and has been obtained from [32]. As mesh a hybrid grid with 17,883 nodes and 21,880 elements (8,357 triangles and 13,523 quads) has been used. The discretization is a full-upwind one, using van Albada's limiter. Integration has been done, using an FAS multi-grid iteration and figure 8.15 shows the convergence history.

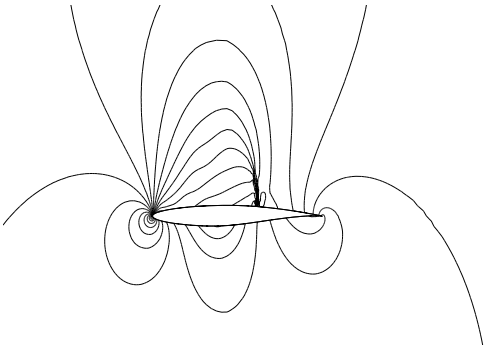

Figure 8.13: Iso-lines of p.

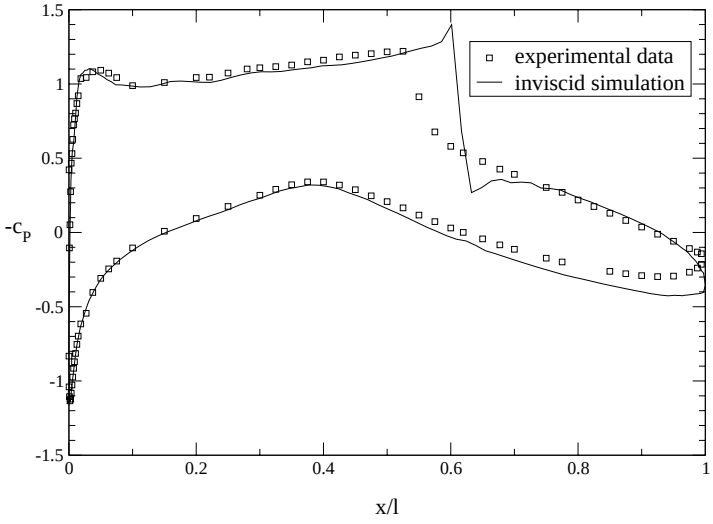

Figure 8.14: $-c_p$ curves.

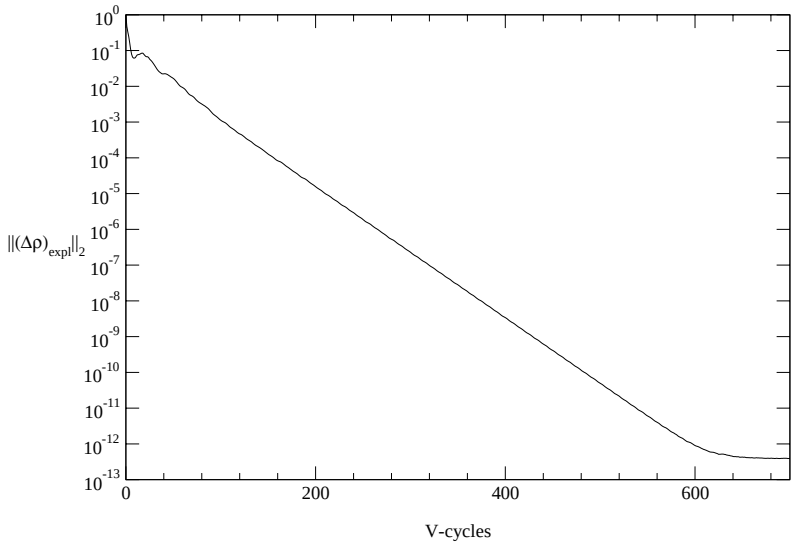

Figure 8.15: Convergence history for 2D/transsonic simulation.

section no.	z/b
1	0.20
2	0.44
3	0.65
4	0.80
5	0.90
6	0.95
7	0.99

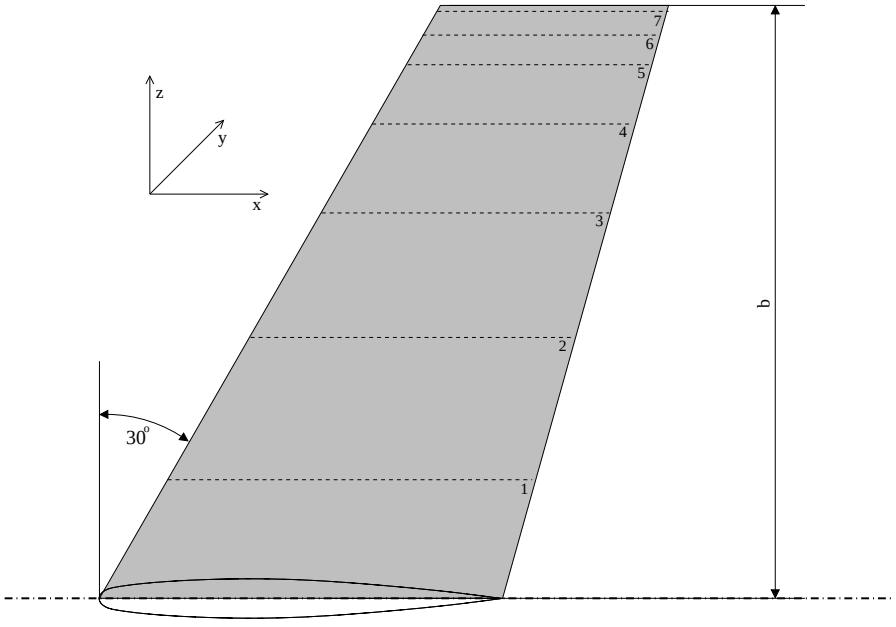

Figure 8.16: ONERA-M6 wing.

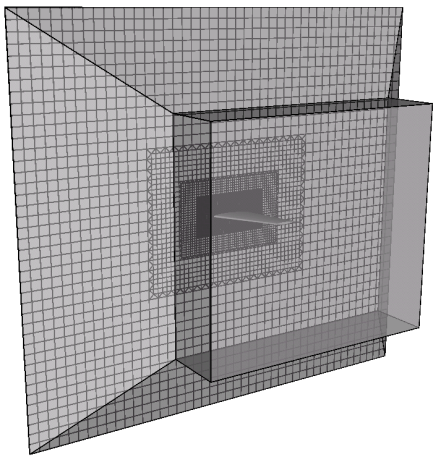

Figure 8.17: Computational Domain.

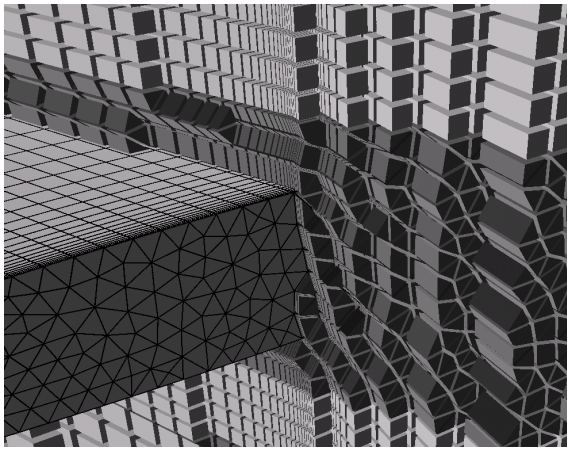

Figure 8.18: Grid Around Wing-Tip.

8.3 Inviscid, Transsonic Flow Past an ONERA-M6 Wing

As a test for three-dimensional transonic flow, an ONERA-M6 wing has been chosen. Experimental data for a free-stream Mach-number of $Ma = 0.8395$ and an angle of attack of 3.06° can be found in [33]. Like the data for the RAE-2822 airfoil the data can be found on the web site [32]. The Reynolds-number of the wind-tunnel tests has been $1.17 \cdot 10^6$, whereas the computational results, which are shown in this work, have been obtained by an inviscid simulation. For an angle of attack of 3.06° no significant seperations occur and thus the computed and experimental pressure values show a good compliance. Figure 8.16 shows a sketch of the swept wing. The seven cross-sections, which have been used

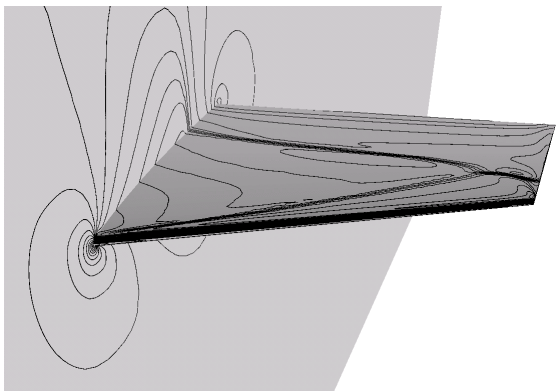

Figure 8.19: Upper side pressure iso-lines.

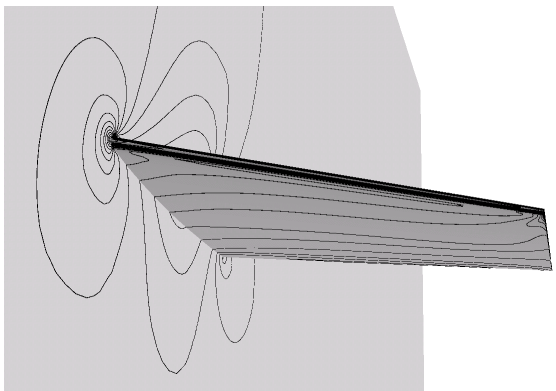

Figure 8.20: Lower side pressure iso-lines.

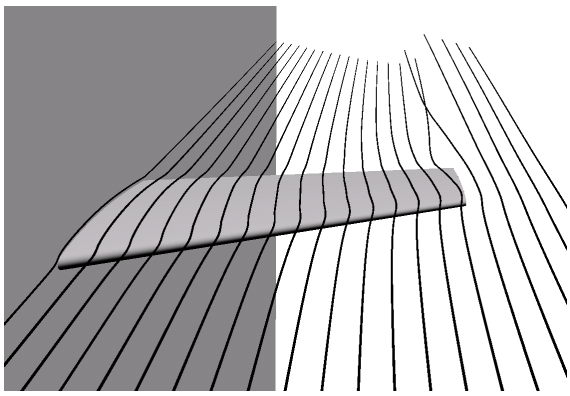

Figure 8.21: Stream-lines.

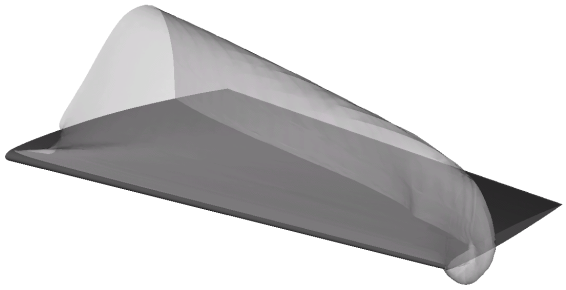

Figure 8.22: Region of $Ma > 1$.

to compare the results, are indicated by dashed lines. Figures 8.19 and 8.20 show iso-plots of the pressure. In figure 8.21 stream-lines can be seen. The experiments, which are described in [33], used a small plate to terminate the wing on the root-side. For the computations the root has been modelled as a plane of symmetry (see figure 8.16). The surface elements of this symmetry-plane can be seen in figure 8.21. Figure 8.22 shows a small part of the unstructured grid around the tip of the wing. Please note that this mesh has been derived from a two-dimensional grid. The whole grid consists of 809,731 nodes and 930,740 elements (285,840 prisms and 644,900 hexahedra). A comparison between measured and computed values for c_P can be found in figures 8.23, 8.24, 8.25, and 8.26. x_0 represents the x-coordinate of the trailing-edge for a section and l the chord-length.

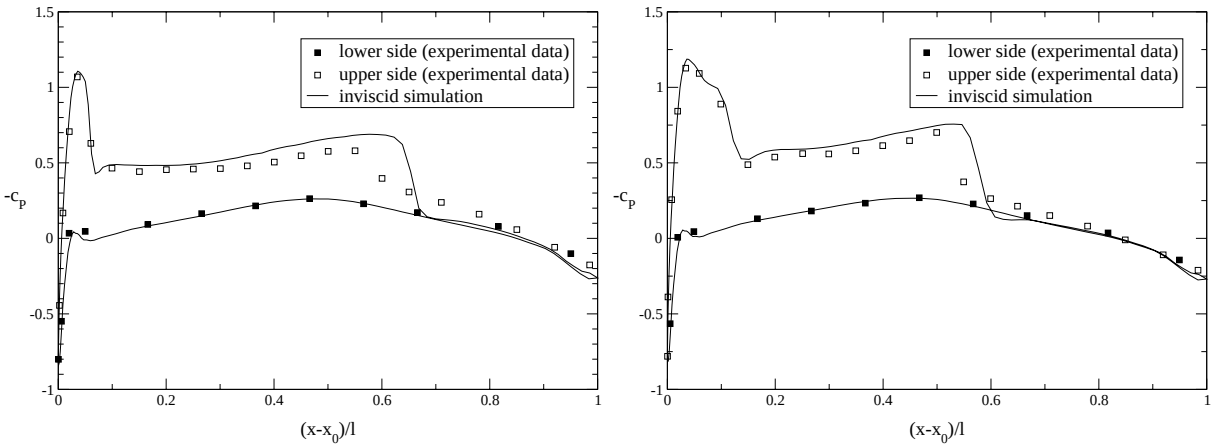

Figure 8.23: Sections 1 and 2 of ONERA-M6 Wing.

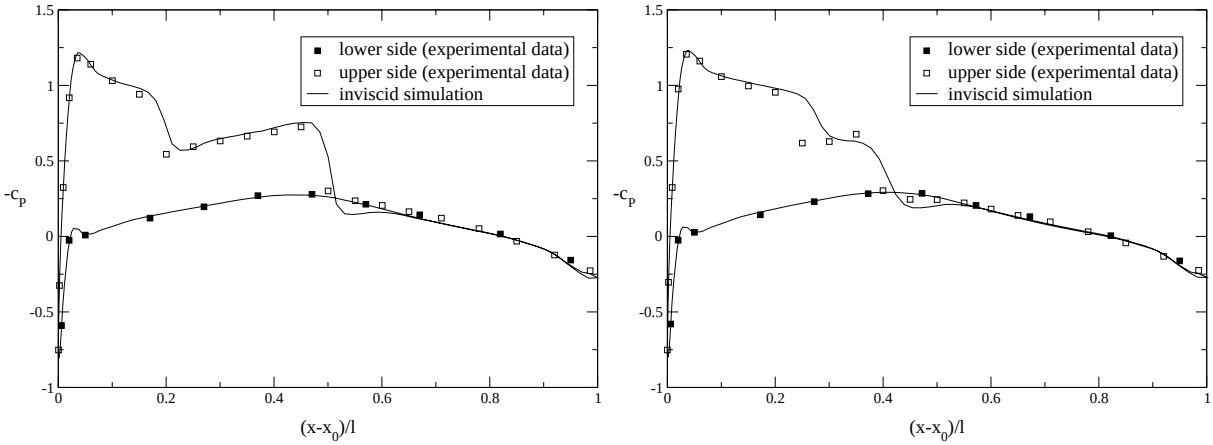

Figure 8.24: Sections 3 and 4 of ONERA-M6 Wing.

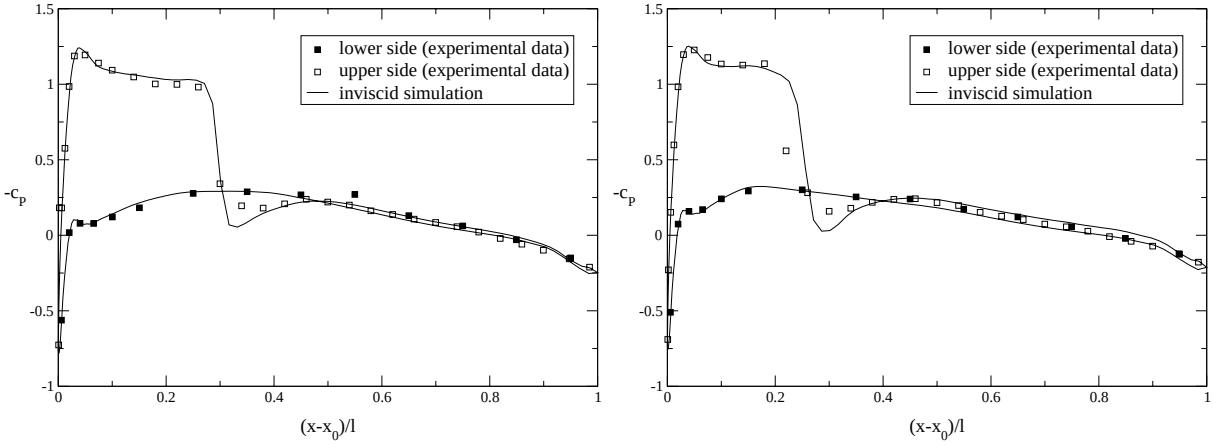

Figure 8.25: Sections 5 and 6 of ONERA-M6 Wing.

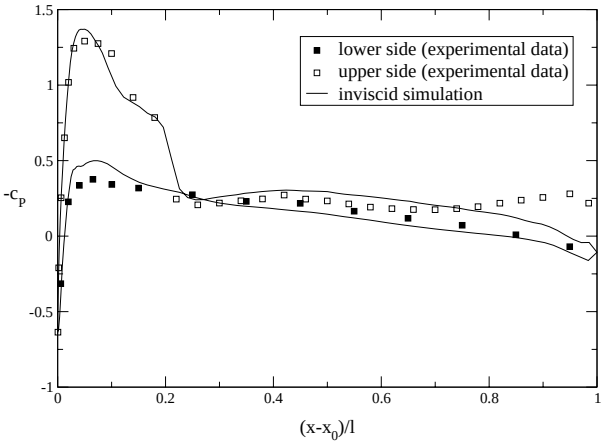

Figure 8.26: Section 7 of ONERA-M6 Wing.